Journal of Materials Chemistry B

ROYAL SOCIETY OF CHEMISTRY

PAPER

View Article Online
View Journal

Cite this: DOI: 10.1039/d6tb00324a

Mechanistic insights into graphene coatings for oral biofilm inhibition and osteoblast compatibility

Xin Chen,[a] Jian Zhang,[a] Shadi Rahimi,[a] Katja Kozjek,[b] Lena Larsson,[c] Ivan Mijakovic[ad] and Santosh Pandit *[a]

The initial adhesion of bacterial cells to implant surfaces is a critical step in biofilm formation. Biofilms are complex microbial communities that are much more tolerant to conventional antimicrobial treatments than planktonic cells, often requiring mechanical disruption in addition to antimicrobial treatment. Once established, these biofilms and their self-produced extracellular matrix are difficult to eradicate. As a result, there is growing interest in engineering implant surfaces that can effectively disrupt bacterial adhesion and subsequent biofilm formation. Various surface-modification strategies, including antimicrobial agents and nanomaterial-based coatings, have been investigated. Among these, graphene-based coatings have shown promising antimicrobial properties. However, the mechanisms of their bactericidal activity remain insufficiently understood. We evaluated the antimicrobial efficacy of vertically aligned graphene (VG) coatings against *Streptococcus mutans*, employing electron microscopy and transcriptomics analysis to elucidate the mode of action. These coatings inhibited biofilm formation through a multifaceted mechanism: (i) reducing bacterial colonization; (ii) mechanical disruption of bacterial membranes by nanoscale protrusions; (iii) modulating expression of the genes associated with membrane integrity, transport, oxidative stress, and cell division. Importantly, the coatings inhibited bacterial adhesion and biofilm formation without affecting osteoblast growth or proliferation. These results indicate that VG coatings could offer a dual benefit by enhancing antimicrobial activity while being compatible for osseointegration, indicating their potential as candidates for next-generation biomedical implants.

Received 7th February 2026,
Accepted 24th May 2026

DOI: 10.1039/d6tb00324a

rsc.li/materials-b

Introduction

Implant-associated infections (IAIs) present a significant global health challenge, contributing to increased morbidity, mortality, and substantial healthcare costs.[1] The prevalence of IAIs can reach up to 30% for certain medical devices.[2] These infections occur when bacteria enter the body through the implant site, adhere to the device surface, and initiate biofilm formation.[3] Biofilms are structured communities of microorganisms encased in a self-produced extracellular matrix, which enables adherence to biological tissues and inert materials.[4,5] In IAIs, bacteria colonize the surfaces of implanted medical devices and secrete extracellular polymeric substances (EPS) that form a protective biofilm matrix, which limits the penetration of antibiotics. Additionally, the formation and aggregation of bacterial cells within the biofilm facilitates collective defence mechanisms, such as the sharing of tolerant genes and localized inactivation of antimicrobials, further enhancing their resilience.[6] This structure enhances bacterial tolerance to antibiotics and evasion from the host immune system, making IAIs fundamentally more difficult to treat than standard infections.[7] While infections caused by planktonic bacteria generally respond to antibiotic therapy aided by immune defences, biofilm-associated infections often persist due to the protective EPS matrix, as well as reduced bacterial metabolic activity and altered gene expression within the biofilm.[7–10]

The rise of antibiotic-tolerant infections represents a major public health challenge worldwide. IAIs are particularly problematic because bacteria can form biofilms on device surfaces, which protect them from antibiotics and the host immune system. These persistent biofilm-associated infections are

[a] Systems and Synthetic Biology Division, Department of Life Sciences, Chalmers University of Technology, SE-412 96, Gothenburg, Sweden. E-mail: pandit@chalmers.se
[b] National Bioinformatics Infrastructure Sweden (NBIS), SciLifeLab, Department of Laboratory Medicine, Lund University, Lund, Sweden
[c] Department of Periodontology, Institute of Odontology Sahlgrenska Academy, University of Gothenburg, Gothenburg, Sweden
[d] The Novo Nordisk Foundation, Center for Biosustainability, Technical University of Denmark, DK-2800 Kogens Lyngby, Denmark

difficult to treat, and often require prolonged therapy or device removal. Preventing bacterial colonization on medical devices is therefore critical, suggesting the need for surface modifications and coatings that can inhibit biofilm formation and improve clinical outcomes. Titanium is one of the most widely used materials for medical implants, valued for its favourable mechanical properties and biocompatibility. However, titanium also has limitations, including a lack of inherent antimicrobial properties. While its surface supports osseointegration, it remains bioinert in terms of preventing bacterial adhesion, making it susceptible to microbial colonization and infection.[11]

To overcome these challenges, researchers have developed advanced surface-modification strategies to enhance osseointegration and antimicrobial performance.[12] These include the incorporation of antimicrobial agents such as silver nanoparticles, antimicrobial peptides, and metal ions, as well as the engineering of nanostructured surfaces that simultaneously promote bone cell adhesion and inhibit bacterial growth.[13–16] Such multifunctional coatings aim to improve implant integration with surrounding bone tissue while reducing infection risk, thereby improving long-term implant success. Among these strategies, surface modifications utilizing antibacterial agents such as quaternary ammonium compounds (QACs) are frequently employed for treating infected bone defects.[17–19] Although QACs exhibit strong antimicrobial properties, a trade-off between antibacterial efficacy and biocompatibility is present.[20] The positive charge and hydrophobicity of QACs can disrupt mammalian cell membranes, leading to cytotoxic effects.[21] This membrane disruption may also trigger oxidative stress and the generation of reactive oxygen species (ROS), which can damage cellular components, promote inflammation, and impair bone healing.[20,21]

An alternative and promising strategy involves mimicking the nanoscale surface structures found on insect wings, such as those of cicadas and dragonflies.[22,23] These natural surfaces contain sharp nanoscale features capable of mechanically rupturing bacterial membranes, thereby preventing bacterial adhesion and biofilm formation without relying on chemical agents. This approach offers a scalable and cost-effective solution for developing antibacterial surfaces on biomedical implants. Hierarchical surface topographies that combine microscale roughness with nanoscale features have been shown to enhance antibacterial activity and biocompatibility.[24,25] Microscale features aid mechanical interlocking with bone tissue to support osseointegration, while nanoscale structures mimic the extracellular matrix to promote cellular interactions and inhibit bacterial adhesion.[26,27] Titanium implants with such micro/nano-structured surfaces have presented improved osteogenic activity and intrinsic antibacterial properties by tailoring surface topography.[28]

In this context, graphene-based coatings with controlled flake density and orientation have recently emerged as a novel approach to deactivate bacterial cells while remaining biocompatible with mammalian cells.[29–31] However, studies have focused predominantly on early-stage bacterial interactions, often testing antimicrobial activity against non-biofilm-forming strains or after only 24 h of bacterial growth, a timeframe insufficient for the development of mature, three-dimensional biofilms. Furthermore, current understanding of the bactericidal activity of graphene is largely limited to its mechanical effects: membrane disruption by sharp flake edges.[29–32] There remains a significant knowledge gap regarding the comprehensive mechanisms of action, including how such surfaces interact with bacterial cell membranes, intracellular components, and broader metabolic processes.

Despite the growing interest in graphene-coated surfaces for biomedical applications, little is known about their effects on mammalian cells, particularly osteoblasts, which are essential for bone regeneration. We hypothesize that graphene-coated surfaces can inhibit bacterial biofilm formation through direct interactions with bacterial cells while supporting osteoblast growth and proliferation. Hence, we investigated the antimicrobial mechanisms of graphene-coated surfaces and evaluated their impact on osteoblast behaviour. *Streptococcus mutans*, a well-characterized oral pathogen known for its robust biofilm-forming ability, was selected as the model organism.[33] We integrated microbiological, microscopic, and transcriptomic approaches to provide a comprehensive, multiscale understanding of how oriented graphene flakes interact with bacterial cell walls, intracellular components such as nucleic acids, and associated stress response pathways. By simultaneously examining these mechanisms alongside osteoblast behaviour, we offer novel insights into the multifaceted functionality of such surfaces indicating their potential to inhibit bacterial activity and support bone-forming cells, thereby advancing the design of multifunctional coatings for biomedical implants.

Experimental

Graphene coatings

VG nanoflakes were synthesized *via* plasma-enhanced chemical vapor deposition (PECVD) using an Aixtron Black Magic system, as described previously.[29] Briefly, substrates consisted of standard p-type silicon wafers coated with a 400 nm layer of silicon dioxide (SiO_2), thermally grown by wet oxidation in an oxyhydrogen atmosphere at 1050 °C. After substrate preparation, the wafers were loaded into a cold-wall CVD chamber and rapidly heated at a rate of approximately 300 °C min^{-1} to a growth temperature of 775 °C. Prior to graphene deposition, the substrates were annealed in a reducing atmosphere consisting of hydrogen and argon. Graphene growth was initiated by igniting a 75-W DC glow discharge plasma, using a gas mixture of 15 sccm acetylene (C_2H_2), 15 sccm hydrogen (H_2), and 1000 sccm argon (Ar).

Evaluation of bacterial growth, biofilm formation and antimicrobial activity

The antimicrobial efficacy of graphene-coated surfaces was assessed using *S. mutans* UA159. Bacterial cultures were grown in brain–heart infusion (BHI) broth supplemented with 1%

glucose, incubated at 37 °C in a humidified atmosphere containing 5% CO_2. To prepare the bacterial inoculum for testing, overnight cultures were diluted in 1% sucrose BHI broth to achieve a final concentration of approximately 2–5 × 10^6 CFU mL^{-1}. A volume of 50 μL of this inoculum was carefully dispensed onto each sample surface (control and graphene-coated substrates) and incubated under the same conditions for 24 h. Following this initial incubation, the medium was replaced with fresh 1% sucrose BHI broth, and incubation was continued for an additional 24 h. Notably, to prevent evaporation of the culture medium from the sample surfaces, the tested samples were placed in the middle part of a 24-well plate, while the surrounding wells and inter-well spaces were filled with sterilized distilled water.

After total incubation of 48 h, biofilms formed on the surfaces were gently rinsed twice with sterile distilled water and transferred into 5 mL of 0.89% NaCl solution. Biofilms were then dislodged and homogenized using probe sonication at 10 W for 30 s, repeated three times. The resulting suspensions were serially diluted and plated onto BHI agar. Colony-forming units (CFUs) were enumerated after 48 h of incubation, and the percentage reduction in viable bacteria was calculated relative to control samples. All experiments were performed in triplicate, and standard deviations represent variation across biological replicates.

Scanning electron microscopy (SEM)

For SEM, 48 h biofilms grown on control and graphene-coated surfaces were fixed in 3% glutaraldehyde for 2 h. Samples were then dehydrated through a graded series of ethanol solutions (40%, 50%, 60%, 70%, 80%, and 90% v/v, each for 10 min), followed by a final dehydration step in 100% ethanol for 20 min. Dehydrated samples were air-dried at room temperature for 2 h. Prior to imaging, a 5 nm gold coating was applied to each sample. SEM was performed using a Supra 60 VP instrument (Carl Zeiss). Three independent biological replicates were analysed for each condition, with five representative fields imaged per replicate.

Confocal laser scanning microscopy (CLSM)

CLSM was used to quantify the extent of live/dead bacterial cells and EPS production by bacterial cells on VG-coated and non-coated surfaces. The 48-h-old biofilms were stained at room temperature in the dark for 30 min using 6.0 μM SYTO 9 and 30 μM propidium iodide (LIVE/DEAD BacLight bacterial viability kit; Molecular Probes, Eugene, OR, USA). CLSM of the biofilms was performed using the A1 system (Nikon) equipped with argon-ion and helium–neon lasers. The excitation wavelengths for SYTO 9 and propidium iodide are 488 and 543 nm, respectively. Three independent experiments were performed, and five image stacks per experiment were collected (n = 10). The bio-volume of live and dead cells was quantified from the entire stack using COMSTAT image-processing software (Heydorn *et al.*, 2000;[34] Pandit *et al.*, 2024[33]). Bio-volume is defined as the volume of the biomass (μm^3) divided by the substratum (SiO_2 surface) area (μm^2).

To examine the EPS and bacterial cells within the biofilm matrix, EPS matrix and bacteria were stained, as described previously.[33] Briefly, 1 μM of Alexa fluor® 647-labeled dextran conjugate was added to the culture medium during biofilm growth to stain exopolysaccharides. After 48 h, these biofilms were exposed to 2.5 μM SYTO® 9 green-fluorescent nucleic acid stain. Two independent experiments were performed and five image stacks (512 × 512 pixels) from five sites per experiment were collected (n = 10). Biofilms (bacterial bio-volume and thickness, and EPS bio-volume and thickness) were quantified from the confocal stacks using COMSTAT.[34]

To assess intracellular ROS, bacterial cells cultured on control and VG-coated surfaces were stained with CellROX™ Deep Red Sensor (Life Technologies) and DAPI. The cells were first incubated with CellROX™ Deep Red dye for 20 min, followed by counterstaining with DAPI for an additional 20 min. Excess dye was removed by washing with sterile water, and the samples were then observed using a fluorescence microscope (Axio Imager Z2m; Zeiss).

Transcriptome analysis

Approximately 2 × 10^7 bacterial cells were harvested at 14 000 × g and rapidly frozen to minimize mRNA degradation. Total RNA was extracted using the RNeasy Mini Kit (Giagen, Germany) following manufacturer instructions. Cells were disrupted with a FastPrep homogenizer (MP Biomedicals, USA), and genomic DNA was removed using DNase I (Invitrogen, USA). The concentration and integrity of RNA were determined with the Qubit RNA HS assay kit (Thermo Fisher Scientific, USA) and the 2100 bioanalyzer (Agilent Technologies, USA), respectively. RNA-seq was performed at the National Genomics Infrastructure of SciLifeLab (Sweden). The raw RNA-seq data are available in the Genome Expression Omnibus (GEO) database (https://www.ncbi.nlm.nih.gov) under BioProject ID: PRJNA1390808.

RNA-seq data were analysed using a Nextflow-based nf-core/rnaseq pipeline (version 3.12.0[35,36]) along with a custom-written Snakemake workflow. Within the nf-core/rnaseq pipeline, FastQC was used to assess the quality of raw FastQ files. Adapter and quality trimming were performed using Trim Galore (https://www.bioinformatics.babraham.ac.uk/projects/trim_galore/). Sequencing reads were then aligned to the reference genome of *S. mutans* UA159 using the STAR RNA-seq aligner.[37] The resulting BAM alignment files were further processed with the custom Snakemake pipeline. Finally, gene-level counts taking into account only coding sequence (CDS) features, were obtained using *featureCounts*.[38]

The downstream analysis of the RNA-sequenced expression data was carried out in R (version 4.3.3). The matrix of the expression data was normalized using the variance stabilizing transformation (VST) implemented in DESeq2 (39) to account for library size differences and within-group variability of low counts. A principal component analysis (PCA) of the normalized expression data was performed to visualize sample clustering and assess similarity/dissimilarity in expression profiles. Differential gene expression analysis was conducted using DESeq2.[39] Genes with an adjusted p-value below

0.05 ($p_{adj} < 0.05$) were considered significantly differentially expressed. These results were visualized using volcano plots. Functional enrichment analysis of differentially expressed (upregulated and downregulated) genes was performed using the enrichR package, which provides an interface to the Enrichr database.[40] We selected the Gene Ontology (GO) database, and all differentially expressed genes were assessed across three categories: biological process (BP), cellular component (CC), and molecular function (MF).

Osteoblast cell growth

The MG63 osteosarcoma cell line (Middlesex University, UK) and human osteoblast cells (HOB-c) were used for toxicity studies. HOB-c was purchased from Sigma (USA). MG63 cells were cultured in Eagle's minimum essential medium (Thermo Scientific) supplemented with 10% fetal bovine serum (Thermo Scientific). HOB-c cells were cultured in osteoblast growth medium (Sigma). Cells were maintained at 37 °C in a humidified atmosphere with 5% CO_2. Control and VG-coated surfaces were placed in 24-well and 48-well plates, and seeded with 8×10^4 and 5×10^4 MG63 and HOB-c cells per well, respectively. The cells were then incubated for 48 h to allow for adhesion and proliferation. After incubation, cells were treated with a medium containing 1× Alamar Blue (Thermo Scientific) staining solution for 4 h. Fluorescence was measured using an OPTIMA BLUE Fluostar plate reader (BMG Labtech, Ortenberg, Germany), and results were normalized against the control.

For SEM, after cell growth for 48 h, samples were fixed using 2.5% of glutaraldehyde for 2 h followed by dehydration with graded series of ethanol solutions (40%, 50%, 60%, 70%, 80%, 90% and 100%) for 10 min each. Dehydrated samples were dried overnight at room temperature. Dried samples were sputter-coated with gold (5 nm) before SEM.

Statistical analyses

All experiments were conducted in triplicate. Data are the mean ± standard deviation (SD). Significance was assessed using a one-way analysis of variance (ANOVA), followed by a *post hoc* multiple comparison (Tukey) test. Unless otherwise specified, biological triplicates were analysed. Significance was defined as $p < 0.05$, unless stated otherwise.

Results and discussion

Graphene coatings and characterization

The synthesis of VG structures *via* plasma-enhanced chemical vapor deposition (PE-CVD) on various substrates has been established in prior studies. For antimicrobial applications, densely packed arrays of VG nanoflakes are essential to effectively disrupt adhered bacterial cells. Research has established that the density, distribution, and height of these nanoflakes are critical parameters that enable physical penetration of bacterial cell walls, leading to the leakage of intracellular contents and subsequent cell deactivation.

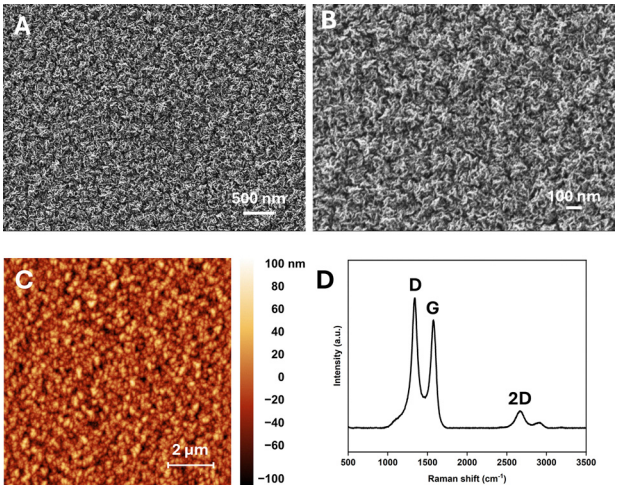

Fig. 1 Physicochemical characterization of the VG coating on the SiO_2 surface. (A) and (B) SEM of VG coatings on the SiO_2 surface from low to higher magnification. (C) Representative 2D AFM topography image of the VG coating. (D) Raman spectrum of the VG coating showing characteristic D, G, and 2D bands.

SEM at different magnifications indicated formation of a VG coating on the SiO_2 substrate (Fig. 1A and B). The low-magnification SEM image showed uniform surface coverage within the observed field of view, while the higher-magnification image depicted a closely packed nanoflake morphology with abundant edge-like features. An additional top-view SEM image is provided in Fig. S1A. These observations indicated that the substrate surface was covered by a continuous and nanostructured VG layer. Cross-sectional SEM showed a continuous VG coating with a vertically oriented nanoflake-like architecture on the substrate (Fig. S1B), providing direct structural evidence for VG growth and additional information on the coating architecture. Further morphological characterization by atomic force microscopy (AFM) showed the nanoscale topography of the VG coating (Fig. 1C). Quantitative AFM analysis showed that the surface exhibited a mean roughness (Sa) of 20.67 nm over a scan area of 10×10 μm^2, suggesting the rough and nanostructured nature of the coating. Additional three-dimensional AFM topography is provided in Fig. S1C.

Raman spectroscopy further showed the graphitic nature of the coating by revealing the characteristic D, G, and 2D bands of graphene (Fig. 1D). The D band at approximately 1350 cm^{-1} indicated structural defects or disorder within the graphene lattice, which is expected for VG due to the high density of exposed edges and grain boundaries. The G band at approximately 1590 cm^{-1} corresponded to the in-plane vibrational mode of sp^2-bonded carbon atoms, and is a characteristic feature of graphitic carbon. The relatively high intensity of the D band compared with that of the G band is consistent with the vertical structure and the high density of flake boundaries and defects. A small 2D peak at approximately 2650 cm^{-1} was also observed, which is consistent with the presence of multilayer graphene structures. Taken together, the SEM, cross-

sectional SEM, AFM, and Raman results indicated formation of a graphitic VG coating with a rough and densely nanostructured surface.

VG coatings protect against *S. mutans* colonization and biofilms growth

Research indicates that microbial colonization of dental biofilms follows a similar pattern on natural teeth and dental implant surfaces.[41] Among the initial colonizers, *S. mutans* plays a prominent part due to its strong adhesive capabilities. Early colonizers such as *S. mutans*, *Actinomyces* spp., and *Streptococcus sobrinus* contribute to the initial stages of biofilm formation by facilitating the attachment and growth of more virulent, periodontopathogenic bacteria, including *Porphyromonas gingivalis* and *Treponema denticola*.[42] Unlike natural teeth, dental implants lack anatomical niches that support bacterial attachment, making the role of early colonizers, particularly *S. mutans*, in initiating biofilm formation on implant surfaces.[43]

Due to this fact, *S. mutans* was selected to evaluate the antimicrobial efficacy and mode of action of VG nanoflake-coated surfaces. The impact of VG on bacterial adhesion and growth was assessed by comparing VG-coated and uncoated control surfaces. After 48 h of incubation, the viability of *S. mutans* on VG-coated surfaces was reduced by 86.1 ± 8.2%, indicating a strong antimicrobial effect (Fig. 2A). This reduction is consistent with previous findings, where viability reductions of 90% and 70% were observed for another Gram-positive bacterium, *Staphylococcus epidermidis*, after 24 and 72 h of growth on VG-coated surfaces, respectively.[29]

S. mutans was cultured in the presence of 1% sucrose to promote adhesion and extracellular matrix production. The glucosyltransferase enzyme produced by *S. mutans* converts dietary sucrose into sticky glucans, which enhance surface adhesion, support co-adhesion of additional pathogenic strains, and contribute to the formation of exopolysaccharide-rich microcolonies.[44] Thus, a biofilm-promoting condition was used to better simulate *in vivo* biofilm development and to assess the real-world antimicrobial potential of VG-coated surfaces.

To further investigate the extent of bacterial adhesion and the physical interactions between bacterial cells and VG surfaces, control and VG-coated samples were examined using SEM after 48 h of *S. mutans* growth. As expected, the control surfaces exhibited dense, three-dimensional biofilm structures with high bacterial cell accumulation (Fig. 2B). In contrast, VG-coated surfaces showed markedly reduced bacterial colonization (Fig. 2B). Moreover, many of the adhered bacterial cells appeared partially or fully ruptured, likely due to mechanical damage caused by the sharp, exposed edges of the VG nanoflakes (Fig. S2).

This physical disruption is consistent with previous reports indicating the bactericidal effect of nanostructured surfaces against a variety of bacterial pathogens through similar mechanisms.[29–31] Notably, even under biofilm-promoting conditions in which *S. mutans* was cultured in the presence of 1% sucrose to enhance adhesion and EPS production, the VG-coated surfaces inhibited bacterial attachment and accumulation significantly. These observations indicated the potential of VG coatings to effectively prevent biofilm formation on implant surfaces.

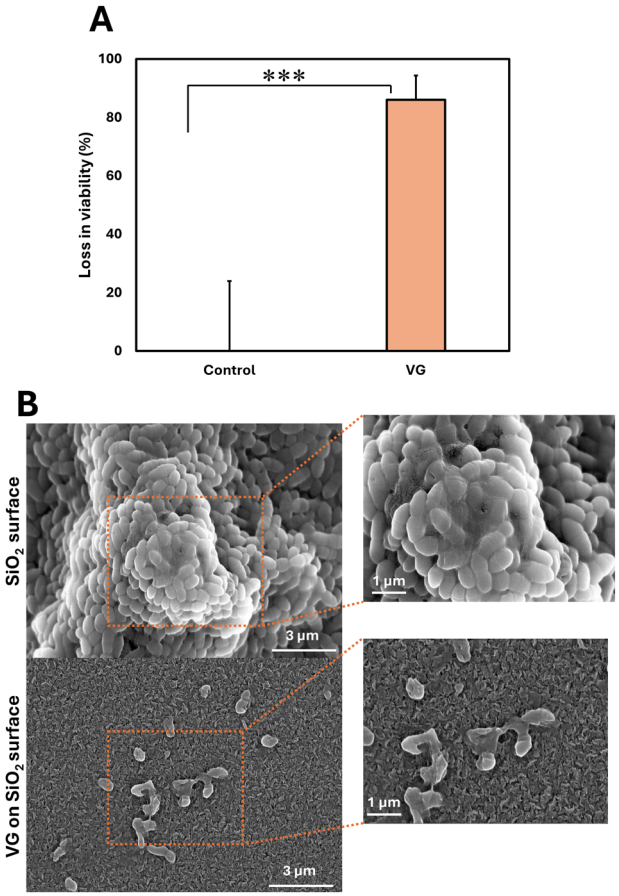

Fig. 2 Antimicrobial efficacy of the VG coating against *S. mutans*. Viability of bacterial cells (%) on control and VG surfaces (A). SEM depicting biofilm growth and bacterial cell morphology in control (SiO_2) and a VG-coated surface (B). Data are the mean ± standard deviation of three individual experiments. ***$p < 0.0001$.

To assess bacterial viability more precisely, live/dead staining was performed after 48 h of growth, followed by CLSM. On control surfaces, most bacterial cells remained viable, with relatively few cells stained by propidium iodide (PI), which selectively labels cells with compromised membranes (Fig. 3A). In contrast, a substantial number of *S. mutans* cells adhered to VG-coated surfaces were stained with PI, indicating a high degree of membrane disruption and cell death (Fig. 3A). To quantify these effects, CLSM images were analysed to determine the total biomass and thickness of live and dead cells within the biofilm matrix (Fig. 3B–E). The biovolume of live cells was significantly reduced on VG-coated surfaces compared with controls (Fig. 3B), while the biovolume of dead cells showed a corresponding increase (Fig. 3C). Similarly, the thickness of live cell populations within the biofilm matrix was significantly lower on VG surfaces (Fig. 3D), whereas the

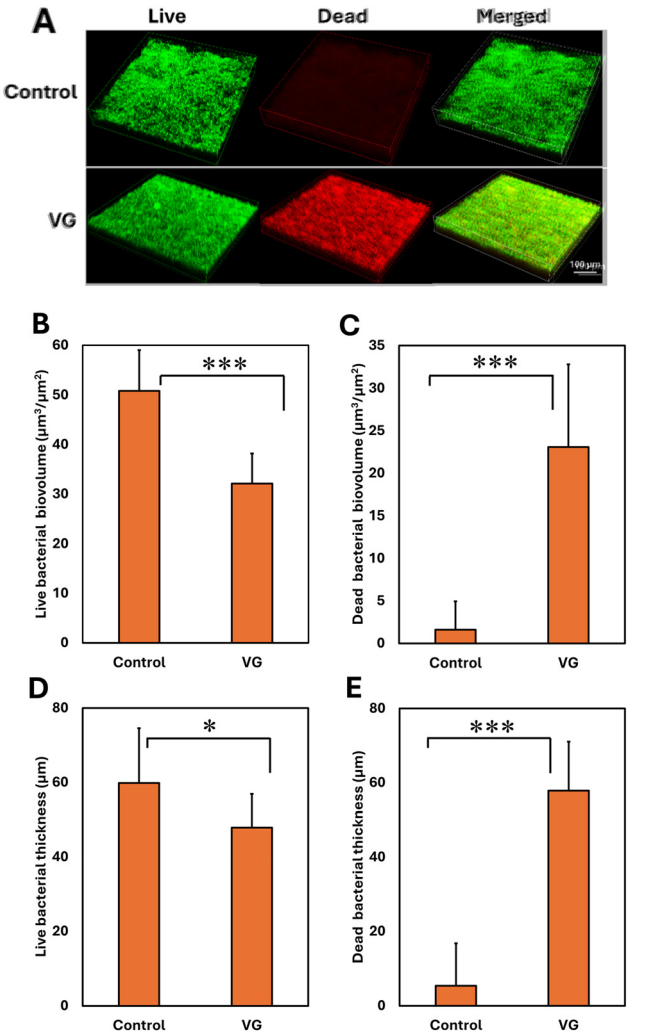

Fig. 3 CLSM of live and dead bacterial cells. Representative 3D CLSM images depicting the density of live and dead cells on a control and VG-coated surface (A). Quantitative analysis of CLSM stack images showing the biovolume of live and dead cells (B) and (C). Thickness of live and dead bacterial cells in the biofilm matrix (D) and (E). Data are the mean ± standard deviation of two individual experiments. *$p < 0.05$; ***$p < 0.0001$.

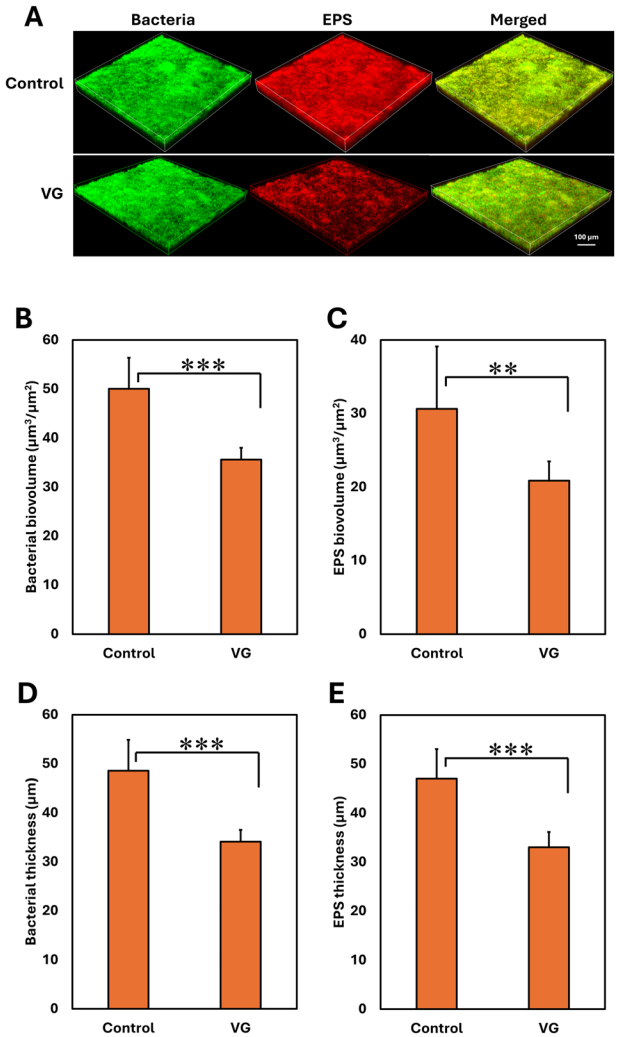

Fig. 4 CLSM for bacterial and EPS content in the biofilm matrix. Representative 3D CLSM images depicting the density and distribution of bacterial cells and EPS on control and a VG-coated surface (A). Quantitative analyses of confocal stack images showing biovolume of bacteria and EPS matrix (B and C). Thickness of bacteria and the EPS matrix in biofilms (D and E). Data are the mean ± standard deviation of two individual experiments. **$p < 0.005$; ***$p < 0.0001$.

thickness of dead bacterial layers was notably higher (Fig. 3E) relative to control surfaces. These findings from live/dead staining were consistent with the SEM observations and bacterial viability assays, collectively indicating the strong antimicrobial and anti-biofilm properties of VG-coated surfaces against *S. mutans*.

Despite the significant bactericidal activity of VG-coated surfaces, a residual layer of live bacterial cells and limited biofilm formation was observed. This suggested that a subset of adhered *S. mutans* cells remained viable and may have produced extracellular polysaccharides (EPS), which facilitated co-adhesion and the formation of bacterial aggregates. To evaluate EPS production on coated and uncoated surfaces, the biofilms were stained using fluorescent markers targeting polysaccharides and nucleic acids, followed by CLSM. As shown in Fig. 4A, VG-coated surfaces exhibited a markedly reduced EPS signal compared with uncoated controls, where bacterial cells were embedded in a well-developed EPS matrix. To quantitatively assess the extent of bacterial adhesion and EPS production, the biovolume and thickness of bacterial cells and EPS were quantified from confocal z-stack images. Consistent with the live/dead staining results, the biovolume and thickness of bacterial cells were significantly reduced on VG-coated surfaces compared with the control (Fig. 4B and D). Similarly, EPS formation was significantly diminished on VG-coated surfaces, as indicated by the lower EPS biovolume and thickness within the biofilm matrix (Fig. 4C and E). These findings suggested that the antimicrobial effect of VG coatings prevented bacterial attachment but also inactivated adhered cells, thereby suppressing the metabolic processes essential for

EPS production. Glucosyltransferase (GTF) enzyme is responsible for synthesizing glucan from dietary sucrose is produced by metabolically active *S. mutans* cells. Hence, any disruption to adhesion or metabolic function directly limits the production of the polysaccharides necessary for mature biofilm development.[45,46]

VG coatings significantly alter the gene expression of adhered bacterial cells

To gain a comprehensive understanding of gene expression changes in *S. mutans* grown on VG-coated surfaces, transcriptomic analysis was performed on bacterial cells from three groups: planktonic cultures (M), cells adhered to uncoated control (SiO_2) surfaces (C), and cells adhered to VG-coated surfaces (S). Principal component analysis (PCA) indicated that *S. mutans* cells on VG-coated surfaces (S) exhibited a distinct gene expression profile compared with planktonic cells (M) and those grown on control surfaces (C) (Fig. S3).

To quantify the extent of transcriptional changes, differential gene expression analysis was conducted between each group. When comparing control surface-adhered cells (C) to planktonic cells (M), 678 genes were differentially expressed (Fig. S4), with 314 genes upregulated and 364 genes downregulated. In comparison, *S. mutans* cells adhered to VG-coated surfaces (S) showed differential expression of 540 genes relative to those on control surfaces (C) (Fig. 5A): 233 upregulated and 307 downregulated genes. When VG-adhered cells (S) were compared directly with planktonic cells (M), 899 genes were differentially expressed (Fig. 5B): 441 upregulated and 458 downregulated genes. Notably, cells grown on VG-coated surfaces exhibited significant numbers of differentially expressed genes compared with planktonic cells and cells grown on the control surface (Fig. 5), indicating the strong transcriptomic response elicited by the nanomaterial. These data supported the hypothesis that VG nanostructures exert their antimicrobial effects through a combination of physical and biochemical interactions.

Differentially expressed genes (DEGs) were further analysed to identify shared expression patterns across experimental groups (Fig. 6 and Fig. S5). The analysis focused on genes with

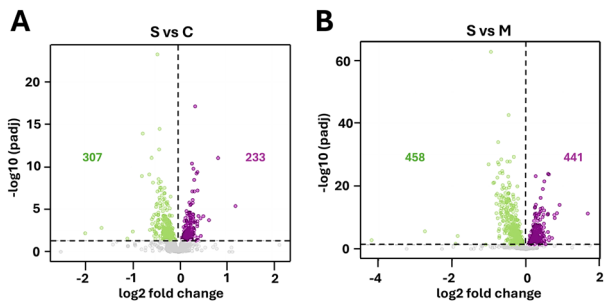

Fig. 5 Volcano plot depicting differentially expressed genes in *S. mutans* cells in a VG-coated surface in compared with a control surface (A) and *S. mutans* cells in a VG-coated surface compared with planktonic cells (B). The horizontal black dotted line represents a significance threshold at p-adj < 0.05.

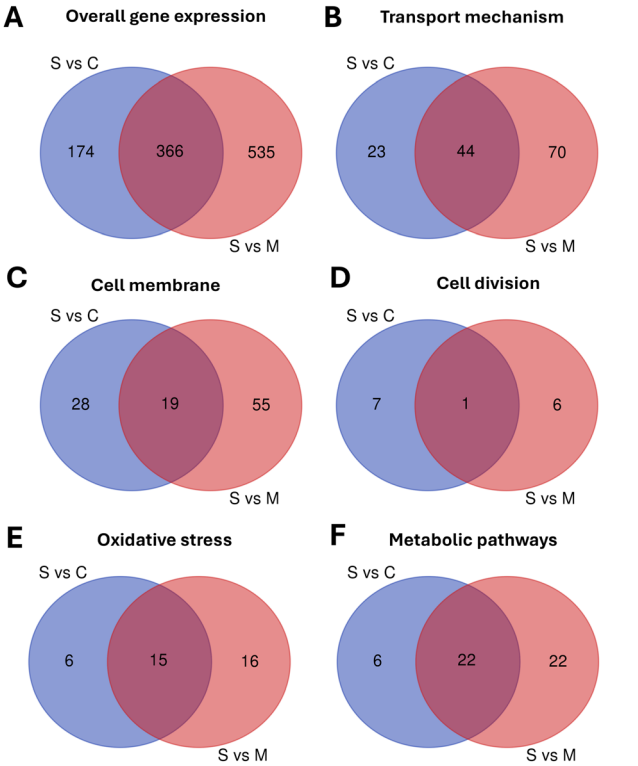

Fig. 6 Venn diagram depicting intersection of data: overlap of significantly regulated all genes (A), genes involved in transport mechanism (B), genes associated to cell membrane (C), genes associated with cell division (D), oxidative stress (E) and genes involved in metabolic pathways (F) between the *S. mutans* cells grown a VG-coated surface *versus* cells grown on a control surface and cells on a VG-coated surface *versus* planktonic *S. mutans* cells.

potential functional relevance in key cellular processes, including membrane transport, cell membrane biosynthesis, cell division, oxidative stress response, and primary metabolic pathways. Among these categories, genes associated with membrane transport and membrane biosynthesis showed the most pronounced differential regulation, followed by those involved in central metabolism, oxidative stress mitigation, and cell cycle progression. Comparative transcriptomic analysis showed a core set of 366 DEGs found to be common in cells grown on a VG-coated surface (S) *versus* cells grown on a control surface (C) and cells grown on a VG-coated surface (S) *versus* planktonic *S. mutans* cells (M) (Fig. 6). Within this shared set, 44 genes were linked to transport mechanisms, 19 to cell membrane biosynthesis, 1 to cell division, 15 to oxidative stress responses, and 22 to primary metabolic functions. These findings are consistent with the known antimicrobial mechanisms of graphene-based materials, which are proposed to disrupt bacterial membranes, impair nutrient and ion transport systems, and induce oxidative stress, ultimately leading to microbial inhibition or inactivation.[31,32]

In the context of mechano-bactericidal activity, hydrophobic nanospikes such as VG physically interact with bacterial membranes, disrupting phospholipid alignment and facilitating membrane penetration or lipid extraction.[47,48] This interaction

can lead to pore formation and loss of membrane integrity. The bacterial cell membrane contains the essential molecular machinery involved in processes such as nutrient transport, metabolite exchange, and cell division, so its disruption can cause leakage of intracellular contents and functional collapse.[47,48] Furthermore, membrane damage triggers excessive production of ROS, resulting in oxidative stress.[49] This redox imbalance can further impair various metabolic and regulatory pathways, contributing to the loss of bacterial viability and function.[49,50] The combined mechanical and oxidative stress responses observed in this study suggest a multifaceted mechanism of action for VG coatings, supporting their potential use in preventing bacterial colonization and biofilm formation on biomedical surfaces.

Gene Ontology (GO) term analysis of transcriptomic data indicated that several carbon metabolism pathways in *S. mutans* were significantly affected when cells were grown on VG-coated surfaces (S) compared with those grown on control surfaces (C) (Fig. S6). In broader comparisons such as VG-coated (S) *versus* planktonic cells (M), a wider range of metabolic pathways was affected. This observation aligns with studies suggesting that bacterial cells within biofilms exhibit markedly different metabolic states and priorities compared with their planktonic counterparts.[51,52] To further explore functional changes, DEGs were categorized based on their roles in key cellular processes and compared across all sample groups (Fig. 7 and Fig. S7). Notably, a distinct subset of genes was significantly upregulated in *S. mutans* cells on VG-coated surfaces compared with control surfaces, indicating specific transcriptional adaptations to the nanostructured environment.

The interaction of VG-coatings with *S. mutans* cells and differentially affected cellular pathways is illustrated in Fig. 8. Among upregulated genes, *thiT* (involved in thiamine transport) and *atpA* (encoding a subunit of the ATP synthase complex) suggest enhanced nutrient uptake and energy production.[52,53] Although specific upregulation of *celB*, *treP*, *lacG*, and *treC* in *S. mutans* biofilms has not been directly reported, related systems, such as tagatose metabolic genes (*lacABCD*, *lacG*) show increased expression in persister cells.[54] This phenomenon supports the underlying premise of enhanced carbohydrate transport and metabolism associated stress responses.[54] The upregulation of *ftsZ*, a key gene regulating cell division, suggests potential stress for enhanced proliferation.[55,56] Additionally, expression of genes linked to the stress response and cell envelope maintenance such as *yaaA*, *mdeA*, *lytR*, and *macP* was increased.[57–59] Broader metabolic reprogramming was suggested by the upregulation of *gltB* (nitrogen metabolism), *carB* (pyrimidine biosynthesis), *galE* (galactose metabolism), and *citC* (citrate metabolism). These changes may reflect increased metabolic flexibility in response to the VG-coated surface, potentially indicating that *S. mutans* cells are adjusting to altered or stressful conditions.

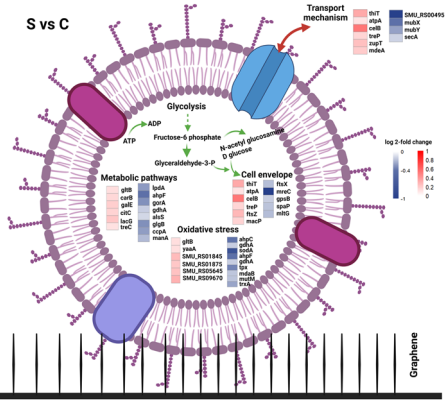

Fig. 8 Schematic illustration depicting interaction of VG-coatings with *S. mutans* cells compared with cells on a non-coated surface (S *vs.* C), along with an overview of affected cellular mechanisms, cell envelope, and stress-related responses.

Conversely, a substantial number of genes were significantly downregulated in *S. mutans* cells on VG-coated surfaces. This included key regulators of cell morphology and division, such as *ftsX*, *mreC*, *gpsB*, and *mltG*, suggesting disruptions in cell wall synthesis and structural maintenance.[60–62] The repression of *spaP*, a major surface adhesin, indicates reduced potential for adhesion and biofilm formation.[63] Additionally, downregulation of genes involved in protein translocation (*secA*) and oxidative stress response—*ahpC*, *sodA*, *tpx*, *mdaB*, *trxA*, and *gorA*—may suggest a possible alteration in redox homeostasis and reduced capacity to manage oxidative stress.[64,65] To verify oxidative stress-associated changes, intracellular ROS levels in bacterial cells grown on control and VG-coated surfaces were examined using CellROX Deep Red staining. Cells grown on the VG-coated surface exhibited markedly enhanced CellROX fluorescence compared with those grown on the control surface, indicating increased oxidative stress induced by the VG coatings (Fig. S8). Although oxidative stress-response genes are typically upregulated under such conditions, their downregulation here may reflect a dysregulated or non-canonical stress response, potentially contributing to ROS accumulation.

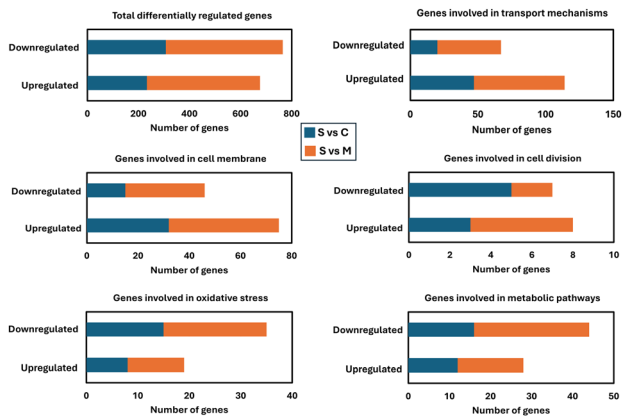

Fig. 7 Number of differentially regulated genes that are associated with transport mechanisms, cell division, oxidative stress, cell membrane synthesis and the genes involved in various metabolic pathways in *S. mutans* grown on a VG surface compared with control surfaces.

Further, expression of genes associated with DNA repair (*mutM*), central carbon metabolism (*gap*, *gdhA*, *alsS*, *manA*), and glycogen biosynthesis (*glgB*) was also suppressed, which may indicate a possible reorganization of metabolic priorities.[66,67] Downregulation of the global metabolic regulator ccpA may be consistent with a broader shift in carbon metabolism.[68] Finally, reduced expression of *mubX*, *mubY*, and *lpdA* suggested a possible downregulation of pathways associated with energy production, cell envelope integrity, and stress response.

Taken together, this gene expression profile may reflect a multifaceted response by *S. mutans* to the VG-coated surface, potentially involving metabolic reprogramming, altered energy expenditure, and modulation of stress response pathways.

Overall, *S. mutans* cells grown on VG-coated surfaces showed upregulation of a range of genes, which may suggest a potentially complex response to this nanostructured environment. These upregulated genes spanned multiple functional categories, including amino acid biosynthesis (*argH*, *trpD*, *metB*, *leuB*, *leuC*, *leuD*, *metG*, *metE*), nucleotide metabolism (*guaA*, *pyrR*), and carbohydrate transport and metabolism (*galT*, *lacC*, *lacD*, *lacG*).[54,69,70] Expression of genes related to protein synthesis and ribosomal function—such as *rplQ*, *rpsK*, *rplE*, *rpmC*, *rplD*, and *rpsJ*—was also upregulated, which may indicate increased translational activity and protein production.[71] Regulatory and stress-response genes, including *nusA*, *hrcA*, *dprA*, and the *brsR*/*brsM* operon, may indicate a coordinated cellular response that could be involved in managing environmental stress and adjusting gene expression accordingly.[72–74] Upregulation of *lytR* and *lytS*, associated with cell envelope remodelling and signal transduction, and *comGF*, involved in competence development, may further support this adaptation.[52,64] Moreover, upregulated expression of central metabolic genes such as *acnA*, *icd*, and *citG* suggests metabolic reprogramming, particularly in carbon metabolism pathways.[75] Collectively, these transcriptomic changes reflect a multifaceted physiological response that could contribute to the survival, metabolic flexibility, and potential virulence on VG-coated surfaces by *S. mutans*.

In contrast, several genes were notably downregulated in *S. mutans* cells grown on VG-coated surfaces, which may suggest a possible reduction in the activity of certain cellular functions. These included genes involved in transcription and DNA replication, such as *rpoE*, *nusB*, *polA*, and *dnaX*, indicating reduced global gene expression and replication activity.[76–78] Expression of genes related to stress response and protein folding—*groL*, *htpX*, *dpr*, and *rpmF*—was also downregulated, possibly reflecting altered protein quality control under the conditions imposed by VG surfaces.[79–81] If stress response genes are downregulated, the ability of cells to neutralize ROS may be impaired, potentially contributing to increased oxidative stress. In turn, the excess ROS could damage regulatory proteins, which may further suppress the expression of stress response genes. Additionally, repression of the genes involved in metal ion homeostasis (*copZ*), sulfur metabolism (*sufD*), and glutathione synthesis (*gshAB*) may suggest possible shifts in redox regulation and the oxidative stress response.[81–83] Genes associated with carbohydrate metabolism and storage (*glgA*, *glgB*, *glgD*, *budA*), as well as genes linked to amino acid biosynthesis (*hisE*, *hisI*, *hisF*), were also suppressed, which may indicate a possible reprioritization of metabolic resources.[84–86] Notably, genes encoding cell division and membrane-associated proteins (*gpsB*, *pbp2b*, *lepB*, *raiA*), along with key regulatory genes such as *sloR* and *hdrM*, were downregulated, which may suggest broader effects on cell envelope integrity and transcriptional control.[61,87–89]

As expected, more genes were differentially expressed in *S. mutans* cells grown on VG-coated surfaces compared with planktonic cells than between VG-coated and uncoated control surfaces. This result is consistent with the well-established physiological differences between planktonic and biofilm-associated cells, which experience distinct environmental cues and mechanical constraints. Among the genes significantly upregulated in cells grown on a VG-surface (S) relative to planktonic cells (M) were those involved in translation and ribosome assembly (*infC*, *prfA*, *rsfS*, *rpmJ*, *rpsH*, *rplC*), which may suggest increased protein synthesis.[90] Genes associated with the stress response and protein folding (*grpE*, *def*) were also upregulated, which may indicate a potential response to surface-associated stress.[91] Genes linked to metabolism and regulation—including *trpE* and *guaB* (amino acid and nucleotide metabolism), *cls* (membrane biosynthesis), and *nmlR*, *sppR*, and *aguA* (transcriptional regulation)—also showed increased expression, which may indicate a broader physiological shift.[54,84,92] Upregulation of hypothetical or poorly characterized genes such as *yqeK* and *yqeH* may suggest the involvement of functions that are not yet well understood and could be related to surface colonization. Conversely, several genes were distinctly downregulated in *S. mutans* cells on VG-coated surfaces relative to planktonic cells, which may further reflect a physiological transition toward a more biofilm-like state. These included genes involved in amino acid biosynthesis and metabolism (*thrC*, *metK*, *ilvD*), which may indicate a reduced demand for *de novo* synthesis.[93,94] Downregulation of *atpD*, a component of the ATP synthase complex, may suggest changes in energy metabolism, potentially reflecting altered or more efficient energy utilization under surface-associated growth conditions.[53] Genes involved in DNA repair and recombination (*recU*, *uvrB*) were also suppressed, which may imply a reduced requirement for DNA maintenance under biofilm conditions.[95] Metabolic genes such as *pflB* (pyruvate formate-lyase) and *fruA* (fructose transporter) were also repressed, which may suggest an altered carbon utilization.[96] Finally, downregulation of global transcriptional regulators such as *purR* and *ciaR* may indicate a broader shift in gene regulatory networks.[97]

Together, these findings indicate a complex, surface-specific transcriptional reprogramming in *S. mutans* exposed to VG-coated surfaces. The observed adaptations may help improve survival, adjust metabolic priorities, and modulate stress responses in response to the antimicrobial and mechanical pressures exerted by the nanostructured surface.

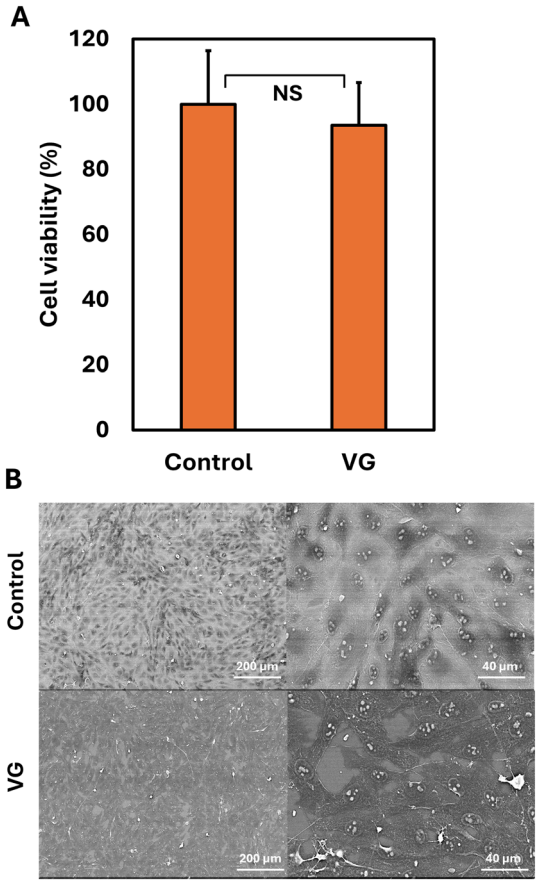

Fig. 9 Biocompatibility of VG-coated surfaces. Viability of osteosarcoma (MG-63) cells on control and VG-coated surfaces after 48 h of growth (A). Representative SEM images of cells on control and VG-coated surfaces (B). NS: not significant ($p > 0.05$).

The VG coating is non-toxic to osteoblast cells

As shown in Fig. 9A, MG63 cells exhibited comparable fluorescence intensities on VG-coated and control surfaces, indicating similar levels of metabolic activity and suggesting that the VG coating did not adversely affect cell viability. This was further supported by SEM data (Fig. 9B), which indicated similar cell density and morphology across both surfaces, indicating healthy attachment and proliferation.

A similar outcome was observed with HOB cells. Viability data (Fig. S9A) and SEM (Fig. S9B) indicated no significant differences in cell adhesion, morphology, or proliferation between VG-coated and control surfaces. These findings collectively indicated the good cytocompatibility of VG coatings with osteoblasts, irrespective of cell type, and support their potential for use in bone-contacting biomedical applications.

Conclusions

This study presents the potent antimicrobial efficacy of VG nanoflake coatings against *S. mutans*, a key early colonizer implicated in biofilm formation on dental implant surfaces. The sharp, VG nanostructures significantly reduced bacterial adhesion, viability, and biofilm formation, even in the presence of sucrose, which typically promotes robust EPS production. SEM and CLSM indicated bacterial membrane damage and reduced EPS matrix development on VG-coated surfaces, supporting the hypothesis that VG induces mechano-bactericidal effects through direct membrane disruption. Transcriptomic profiling provided further mechanistic insight, indicating wide alterations in gene expression in response to VG surfaces. Upregulation of the genes involved in stress response, translation, and central metabolism may indicate an adaptive shift related to survival under surface-imposed mechanical and oxidative stress. Conversely, downregulation of genes related to cell division, membrane biosynthesis, oxidative stress defense, and metabolic activity reflects a potentially altered physiological state and possible reduction in virulence potential in *S. mutans*.

Collectively, these findings indicate that VG coatings, which combine mechanical bactericidal effects with potential metabolic interference, may represent a promising approach for addressing implant-associated infections. The reported biocompatibility of VG surfaces with osteoblasts further supports their potential for use in next-generation biomedical implants with antimicrobial properties and improved osseointegration. However, it is important to note that this study relied on a static droplet mono-species biofilm model which, despite efforts to control evaporation, has inherent limitations. Specifically, this model does not replicate nutrient gradients, fluid flow, or the complex multispecies interactions typical of clinical biofilms, limiting the direct translational relevance of the results. Therefore, future studies should employ multispecies biofilm models under dynamic flow conditions and evaluate long-term *in vivo* performance and host immune responses to more rigorously assess the clinical applicability of VG-nanostructured coatings.

Author contributions

Xin Chen: writing, investigation, data analyses. Jian Zhang: writing (review and editing), investigation. Shadi Rahimi: writing, investigation. Katja Kozjek: analysis of RNA sequencing. Lena Larsson: writing (review and editing). Ivan Mijakovic: supervision, funding acquisition. Santosh Pandit: conceptualization, writing (review and editing), supervision, funding acquisition.

Conflicts of interest

There are no conflicts to declare.

Data availability

The data will be available on request.

Supplementary information (SI): containing additional SEM analysis of VG surface, damaged bacterial cell morphology due to VG, PCA analysis, volcano plot, overlap of regulated genes among experimental groups, GO enrichment analysis, differentially

regulated genes linked to metabolic pathways, fluorescence microscopic images of ROS staining and human osteoblast cell viability in control and VG coated surfaces. See DOI: https://doi.org/10.1039/d6tb00324a.

The raw RNA-seq data are available in the Genome Expression Omnibus (GEO) database (https://www.ncbi.nlm.nih.gov) under BioProject ID: PRJNA1390808.

Acknowledgements

This work was supported by grants from Vetenskapsrådet (2020-04096) and VINNOVA (2023-04134) to SP, and NNF (NNF20CC0035580) to IM. Part of this work was carried out in Chalmers Materials Analysis Laboratory (CMAL). The authors acknowledge the SNP&SEQ Technology Platform National Genomics Infrastructure (NGI) Science for Life Laboratory, Uppsala University, and National Bioinformatics Infrastructure (NBIS) Sweden for their support in RNA sequencing and data analysis. Data handling was enabled by resources in project naiss2024-23-66 provided by the National Academic Infrastructure for Supercomputing in Sweden (NAISS) at UPPMAX, funded by the Swedish Research Council through a grant (2022-06725).

Notes and references

1 J. Sahoo, S. Sarkhel, N. Mukherjee and A. Jaiswal, *ACS Omega*, 2022, **7**, 45962–45980.
2 A. Trampuz and W. Zimmerli, *Injury*, 2006, **37**, S59–S66.
3 S. Cometta, D. W. Hutmacher and L. Chai, *Biomaterials*, 2024, **309**, 122578.
4 H. C. Flemming and J. Wingender, *Nat. Rev. Microbiol.*, 2010, **8**, 623–633.
5 I. Guzmán-Soto, C. McTiernan, M. Gonzalez-Gomez, A. Ross, K. Gupta, E. J. Suuronen, T. F. Mah, M. Griffith and E. I. Alarcon, *Iscience*, 2021, **24**, 102443.
6 V. Nandakumar, S. Chittaranjan, V. M. Kurian and M. Doble, *Polym. J.*, 2013, **45**, 137–152.
7 C. R. Arciola, D. Campoccia and L. Montanaro, *Nat. Rev. Microbiol.*, 2018, **16**, 397–409.
8 S. Sharif and A. K. Yadav, *Microbe*, 2025, 100356.
9 D. Sharma, L. Misba and A. U. Khan, *Antimicrob. Resist. Infect. Control*, 2019, **8**, 76.
10 H. Y. Liu, E. L. Prentice and M. A. Webber, *npj Antimicrob. Resist.*, 2024, **2**, 27.
11 J. Quinn, R. McFadden, C. W. Chan and L. Carson, *IScience*, 2020, **23**, 11.
12 P. Yuan, M. Chen, X. Lu, H. Yang, L. Wang, B. Tian, W. Zhou, T. Liu and S. Yu, *J. Mater. Chem. B*, 2024, **12**, 10516–10549.
13 M. C. Cortizo, T. G. Oberti, M. S. Cortizo, A. M. Cortizo and M. A. F. L. de Mele, *J. Dent.*, 2012, **40**, 329–337.
14 M. Thukkaram, M. Vaidulych, O. Kylian, J. Hanus, P. Rigole, S. Aliakbarshirazi, M. Asadian, A. Nikiforov, A. Van Tongel, H. Biederman, T. Coenye, G. Du Laing, R. Morent, L. De Wilde, K. Verbeken and N. De Geyter, *ACS Appl. Mater. Interfaces*, 2020, **12**, 23655–23666.
15 K. V. Holmberg, M. Abdolhosseini, Y. Li, X. Chen, S. U. Gorr and C. Aparicio, *Acta Biomater.*, 2013, **9**, 8224–8231.
16 Y. Yao, P. Lin, D. Ye, H. Miao, L. Cao, P. Zhang, J. Xu and L. Dai, *Int. J. Nanomed.*, 2025, **20**, 3749–3764.
17 Y. Jiao, L. N. Niu, S. Ma, J. Li, F. R. Tay and J. H. Chen, *Prog. Polym. Sci.*, 2017, **71**, 53–90.
18 L. Cheng, K. Zhang, N. Zhang, M. A. S. Melo, M. D. Weir, X. D. Zhou, Y. X. Bai, M. A. Raynolds and H. H. K. Xu, *J. Dent. Res.*, 2017, **96**, 855–863.
19 C. Z. Abid, S. Jain, R. Jackeray, S. Chattopadhyay and H. Singh, *J. Biomed. Mater. Res., Part B*, 2017, **105**, 521–530.
20 S. Mohapatra, L. Yutao, S. G. Goh, C. Ng, Y. Luhua, N. H. Tran and K. Y. H. Gin, *J. Hazard. Mater.*, 2023, **445**, 130393.
21 W. A. Arnold, A. Blum, J. Branyan, T. A. Bruton, C. C. Carignan and G. Cortopassi, *et al.*, *Environ. Sci. Technol.*, 2023, **57**, 7645–7665.
22 S. M. Kelleher, O. Habimana, J. Lawler, B. O'Rilly, S. Daniels, E. Casey and A. Cowley, *ACS Appl. Mater. Interfaces*, 2016, **8**, 14966–14974.
23 D. E. Mainwaring, S. H. Nguyen, H. Webb, T. Jakubov, M. Tobin, R. N. Lamb, A. H. F. Wu, R. Marchant, R. J. Crawford and E. P. Ivanova, *Nanoscale*, 2016, **8**, 6527–6534.
24 T. Sjöström, A. H. Nobbs and B. Su, *Mater. Lett.*, 2016, **167**, 22–26.
25 G. Hazell, P. W. May, P. Taylor, A. H. Nobbs, C. C. Welch and B. Su, *Biomater. Sci.*, 2018, **6**, 1424–1432.
26 N. Rousseau, I. Msolli, P. Chabrand, A. Destainville, O. Richart and J. L. Milan, *J. Periodontal Res.*, 2021, **56**, 789–803.
27 R. Li, S. Li, Y. Zhang, D. Jin, Z. Lin, X. Tao, T. Chen, L. Zheng, Z. Zhang and Q. Wu, *Front. Bioeng. Biotechnol.*, 2023, **11**, 1223339.
28 T. Ziegelmeyer, K. M. de Sousa, T. Y. Liao, R. Lartizien, A. Delay, J. Vollaire, V. Josserand, D. Linklater, P. H. Le, J. L. Coll, G. Bettega, E. P. Ivanova and V. Martel-Frachet, *Mater. Today Bio*, 2025, **32**, 101710.
29 S. Pandit, Z. Cao, V. R. S. S. Mokkapati, E. Celauro, A. Yurgens, M. Lovmar, F. Westerlund, J. Sun and I. Mijakovic, *Adv. Mater. Interfaces*, 2018, **5**, 1701331.
30 S. Pandit, K. Gaska, V. R. S. S. Mokkapati, E. Celauro, A. Derouiche, S. Forsberg, M. Svensson, R. Kádár and I. Mijakovic, *Small*, 2020, **16**, 1904756.
31 Y. Chen, S. Pandit, S. Rahimi and I. Mijakovic, *Carbon*, 2024, **218**, 118740.
32 W. Wei, J. Li, Z. Liu, Y. Deng, D. Chen, P. Gu, G. Wang and X. Fan, *J. Mater. Chem. B*, 2020, **8**, 6069–6079.
33 S. Pandit, M. A. Kim, J. E. Jung, H. M. Choi and J. G. Jeon, *Biofilm*, 2024, **8**, 100241.
34 A. Heydorn, A. T. Nielsen, M. Hentzer, C. Sternberg, M. Givskov, B. K. Ersbøll and S. Molin, *Microbiology*, 2000, **146**, 2395–2407.

35 P. A. Ewels, A. Peltzer, S. Fillinger, H. Patel, J. Alneberg, A. Wilm, M. U. Garcia, P. D. Tommaso and S. Nahnsen, *Nat. Biotechnol.*, 2020, **38**, 276–278.
36 H. Patel, P. Ewels, A. Peltzer, O. Botvinnik, G. Sturm, D. Moreno, P. Vemuri, M. U. Garcia, L. Pantano, M. Binzer-Panchal, N. C. Bot, R. Syme, M. Zepper, G. Kelly, F. Hanssen, Y. J. A. Fellows, C. Cheshire, J. Espinosa-Carrasco, E. Miller, A. Talbot, P. Zhou, S. Guinchard, M. Hörtenhuber, G. Gabernet, C. Mertes, D. Straub and P. D. Tommaso, *Zenodo*, 2023.
37 A. Dobin, C. A. Davis, F. Schlesinger, J. Drenkow, C. Zaleski, S. Jha, P. Batut, M. Chaisson and T. R. Gingeras, *Bioinformatics*, 2013, **29**, 15–21.
38 Y. Liao, G. K. Smyth and W. Shi, *Bioinformatics*, 2014, **30**, 923–930.
39 M. I. Love, W. Huber and S. Anders, *Genome Biol.*, 2014, **15**, 550.
40 Z. Xie, A. Bailey, M. V. Kuleshov, D. J. B. Clarke, J. E. Evangelista, S. L. Jenkins, A. Lachmann, M. L. Wojciechowicz, E. Kropiwnicki, K. M. Jagodnik, M. Jeon and A. Ma'ayan, *Curr. Protoc.*, 2021, **1**, e90.
41 Y. Wei, G. P. Dang, Z. Y. Ren, M. C. Wan, C. Y. Wang, H. B. Li, T. Zhang, F. R. Tay and L. N. Niu, *NPJ Bionfilms Microbi.*, 2024, **10**, 56.
42 M. Feldman, W. S. Moustafa Elsayed, M. Friedman, I. Gati, D. Steinberg and H. Marei, *Int. J. Dent.*, 2022, **1**, 7246155.
43 A. S. Meza-Siccha, M. A. Aguilar-Luis, W. Silva-Caso, F. Mazulis, C. Barragan-Salazar and J. del Valle-Mendoza, *Int. J. Dent.*, 2019, **1**, 4292976.
44 J. A. Lemos, S. R. Palmer, L. Zeng, Z. T. Wen, J. K. Kajfasz, I. A. Freires, J. Abranches and L. J. Brady, *Microbiol. Spectr.*, 2019, **7**, 10–1128.
45 H. Koo, J. Xiao, M. I. Klein and J. G. Jeon, *J. Bacteriol.*, 2010, **192**, 3024–3032.
46 Q. Zhang, Q. Ma, Y. Wang, H. Wu and J. Zou, *Int. J. Oral Sci.*, 2021, **13**, 30.
47 Y. Tu, M. Lv, P. Xiu, T. Huynh, M. Zhang, M. Castelli, Z. Liu, Q. Huang, C. Fan, H. Fang and R. Zhou, *Nat. Nanotechnol.*, 2013, **8**, 594–601.
48 D. P. Linklater, V. A. Baulin, S. Juodkazis and E. P. Ivanova, *Interface Focus*, 2018, **8**, 20170060.
49 S. Liu, T. H. Zeng, M. Hofmann, E. Burcombe, J. Wei, R. Jiang, J. Kong and Y. Chen, *ACS Nano*, 2011, **5**, 6971–6980.
50 N. Parvin, S. W. Joo and T. K. Mandal, *Antibiotics*, 2025, **14**, 207.
51 M. Shemesh, A. Tam and D. Steinberg, *Microbiology*, 2007, **153**, 1307–1317.
52 M. Afzal, M. Carda-Diéguez, S. Bloch, L. G. Thies, A. Mira and C. Schäffer, *Front. Oral Health*, 2025, **6**, 1535034.
53 M. I. Klein, J. Xiao, B. Lu, C. M. Delahunty, J. R. Yates III and H. Koo, *PLoS One*, 2012, **7**, e45795.
54 D. Dufour, H. Li, S. G. Gong and C. M. Lévesque, *Genes*, 2023, **14**, 1887.
55 Y. Chen, Y. Li, C. Yuan, S. Liu, F. Xin, X. Deng and X. Wang, *Mol. Oral Microbiol.*, 2022, **37**, 97–108.
56 K. Moon, S. Hwang, H. J. Lee, E. Jo, J. N. Kim and J. Cha, *Front. Microbiol.*, 2022, **13**, 945023.
57 Y. Li, D. Qiao, Y. Zhang, W. Hao, Y. Xi, X. Deng, X. Ge and M. Xu, *Mol. Oral Microbiol.*, 2021, **36**, 295–307.
58 R. Nagasawa, T. Sato, N. Nomura, T. Nakamura and H. Senpuku, *Appl. Environ. Microbiol.*, 2020, **86**, e00770–20.
59 L. A. Vega, M. Sanson-Iglesias, P. Mukherjee, K. D. Buchan, G. Morrison, A. E. Hohlt and A. R. Flores, *Antimicrob. Agents Chemother.*, 2024, **68**, e00496-24.
60 H. C. T. Tsui, J. J. Zheng, A. N. Magallon, J. D. Ryan, R. Yunck, B. E. Rued, T. G. Bernhardt and M. E. Winkler, *Mol. Microbiol.*, 2016, **100**, 1039–1065.
61 L. R. Hammond, M. D. Sacco, S. J. Khan, C. Spanoudis, A. Hough-Neidig, Y. Chen and P. J. Eswara, *Microbiol. Spectr.*, 2022, **10**, e01413–e01422.
62 A. Galinier, C. Delan-Forino, E. Foulquier, H. Lakhal and F. Pompeo, *Biomolecules*, 2023, **13**, 720.
63 Z. T. Wen, D. Yates, S. J. Ahn and R. A. Burne, *BMC Microbiol.*, 2010, **10**, 111.
64 J. P. Bitoun, S. Liao, X. Yao, S. J. Ahn, R. Isoda, A. H. Nguyen, L. J. Brady, R. A. Burne, J. Abranches and Z. T. Wen, *Appl. Environ. Microbiol.*, 2012, **78**, 2914–2922.
65 J. K. Kajfasz, T. Ganguly, E. L. Hardin, J. Abranches and J. A. Lemos, *Sci. Rep.*, 2017, **7**, 16018.
66 J. Liu, C. Wu, I. H. Huang, J. Merritt and F. Qi, *Microbiology*, 2011, **157**, 2433–2444.
67 J. L. Baker, J. Abranches, R. C. Faustoferri, C. J. Hubbard, J. A. Lemos, M. A. Courtney and R. Quivey Jr, *Mol. Oral Microbiol.*, 2015, **30**, 496–517.
68 J. Abranches, M. M. Nascimento, L. Zeng, C. M. Browngardt, Z. T. Wen, M. F. Rivera and R. A. Burne, *J. Bacteriol.*, 2008, **190**, 2340–2349.
69 J. Kong, K. Xia, X. Su, X. Zheng, C. Diao, X. Yang, X. Zuo, J. Xu and X. Liang, *AMB Express*, 2021, **11**, 102.
70 M. Jing, T. Zheng, T. Gong, J. Yan, J. Chen, Y. Lin, B. Tang, Q. Ma, X. Zhou and Y. Li, *Microbiol. Spectr.*, 2022, **10**, e00721–e00722.
71 C. Eymann, G. Homuth, C. Scharf and M. Hecker, *J. Bacteriol.*, 2002, **184**, 2500–2520.
72 J. A. Lemos, Y. Y. M. Chen and R. A. Burne, *J. Bacteriol.*, 2001, **183**, 6074–6084.
73 Z. Xie, T. Okinaga, G. Niu, F. Qi and J. Merritt, *Mol. Microbiol.*, 2010, **78**, 1431–1447.
74 K. Fujishima, M. Kawada-Matsuo, Y. Oogai, M. Tokuda, M. Torii and H. Komatsuzawa, *Appl. Environ. Microbiol.*, 2013, **79**, 1436–1443.
75 J. S. Chia, Y. Y. Lee, P. T. Huang and J. Y. Chen, *Infect. Immun.*, 2001, **69**, 2493–2501.
76 X. Xue, J. Tomasch, H. Sztajer and I. Wagner-Döbler, *J. Bacteriol.*, 2010, **192**, 5081–5092.
77 A. C. Len, D. W. Harty and N. A. Jacques, *Microbiology*, 2004, **150**, 1339–1351.
78 M. W. Sherman, S. Sandeep and L. M. Contreras, *ACS Synth. Biol.*, 2021, **10**, 1024–1038.
79 Z. T. Wen, P. Suntharaligham, D. G. Cvitkovitch and R. A. Burne, *Infect. Immun.*, 2005, **73**, 219–225.

80 A. C. Len, D. W. Harty and N. A. Jacques, *Microbiology*, 2004, **150**, 1339–1351.
81 X. Cheng, X. Xu, X. Zhou and J. Ning, *J. Oral Microbiol.*, 2024, **16**, 2292539.
82 S. S. Garcia, Q. Du and H. Wu, *Mol. Oral Microbiol.*, 2016, **31**, 515–525.
83 K. Ellepola, X. Huang, R. P. Riley, J. P. Bitoun and Z. T. Wen, *Front. Microbiol.*, 2021, **12**, 671533.
84 B. E. Costa Oliveira, A. P. Ricomini Filho, R. A. Burne and L. Zeng, *Front. Microbiol.*, 2021, **12**, 636684.
85 Z. D. Moye, L. Zeng and R. A. Burne, *Appl. Environ. Microbiol.*, 2014, **80**, 972–985.
86 L. Yang, Y. Chen, Y. Chi, X. Chen, Y. Zhao, M. Zhang, X. Wang, Y. Li, J. Nie and X. Wang, *J. Oral Microbiol.*, 2025, **17**, 2533174.
87 F. Pompeo, E. Foulquier, B. Serrano, C. Grangeasse and A. Galinier, *Mol. Microbiol.*, 2015, **97**, 139–150.
88 H. C. T. Tsui, M. J. Boersma, S. A. Vella, O. Kocaoglu, E. Kuru, J. K. Peceny, E. E. Carlson, M. S. VanNieuwenhze, Y. V. Brun, S. L. Shaw and M. E. Winkler, *Mol. Microbiol.*, 2014, **94**, 21–40.
89 K. P. O'Rourke, J. D. Shaw, M. W. Pesesky, B. T. Cook, S. M. Roberts, J. P. Bond and G. A. Spatafora, *J. Bacteriol.*, 2010, **192**, 1433–1443.
90 P. Treerat, C. de Mattos, M. Burnside, H. Zhang, Y. Zhu, Z. Zou, D. Anderson, H. Wu, J. Merritt and J. Kreth, *J. Bacteriol.*, 2024, **206**, e00104–e00124.
91 J. A. Lemos, Y. Luzardo and R. A. Burne, *J. Bacteriol.*, 2007, **189**, 1582–1588.
92 M. E. MacGilvray, J. D. Lapek Jr, A. E. Friedman and R. G. Quivey Jr, *Microbiology*, 2012, **158**, 2133–2143.
93 B. Santiago, M. Marek, R. C. Faustoferri and R. G. Quivey Jr, *J. Bacteriol.*, 2013, **195**, 3552–3562.
94 G. A. Ashniev, S. N. Petrov and S. N. Iablokov, *Microorganisms*, 2022, **10**, 740.
95 M. I. Klein, L. DeBaz, S. Agidi, H. Lee, G. Xie, A. H. M. Lin, B. R. Hamaker, J. A. Lemos and H. Koo, *PLoS One*, 2010, **5**, e13478.
96 L. Zeng, Z. T. Wen and R. A. Burne, *Mol. Microbiol.*, 2006, **62**, 187–200.
97 C. Wu, E. A. Ayala, J. S. Downey, J. Merritt, S. D. Goodman and F. Qi, *J. Bacteriol.*, 2010, **192**, 4669–4679.